designs

MDPI

Article

Optimizing Beam Stiffness and Beam Modal Response with Variable Spacing and Extrusion (VaSE)

Patrick N. Murphy, Richard A. Vittum III and Bashir Khoda *

Department of Mechanical Engineering and Advanced Structures and Composites Center, The University of Maine, Orono, ME 04469, USA; patrick.n.murphy@maine.edu (P.N.M.); richard.vittum@maine.edu (R.A.V.III)
* Correspondence: bashir.khoda@maine.edu

Abstract: This paper presents a novel algorithm, Variable Spacing and Extrusion (VaSE), designed to optimize the infill pattern of material extrusion (ME) 3D-printed parts for specified mechanical performance while ensuring manufacturability. The algorithm adjusts deposition spacing and width across layers to achieve functionally graded infill distributions derived from input density maps. First, the variable line spacing algorithm is implemented by normalizing the weighted density distribution. Errors in between the desired density and the density from the line spacing are corrected with a varying extrusion width algorithm. Two application scenarios are demonstrated with the proposed VaSE algorithm. First, beam samples are optimized for flexural stiffness and tested under three-point bending, showing a 10.8–19.2% stiffness increase compared to homogeneous infill, except at low (25%) volume fractions, where local buckling dominated failure. The second scenario involves maximizing the frequency of the first three modes of beams under an induced vibration. The optimized beams, taken straight from a topology optimization algorithm performed in the ANSYS 2023 finite element software, were compared to the beams that were instead put through the VaSE algorithm after the topology optimization. While all manufactured beams underperform relative to simulation, the VaSE-optimized beams show substantial frequency gains (34–63% for the first mode, 0.82–65% for the second mode) over purely geometry-based designs, with the exception of high-mass-fraction beams. These findings highlight the significance of the VaSE algorithm in enhancing mechanical performance and extending the design space of ME additive manufacturing beyond conventional homogeneous infill strategies.

Keywords: additive manufacturing; material extrusion; infill; topology optimization; functionally graded lattice structure; manufacturability; beam stiffness; modal response

check for updates

Academic Editor: Diana Popescu

Received: 20 April 2025
Revised: 14 May 2025
Accepted: 14 May 2025
Published: 19 May 2025

Citation: Murphy, P.N.; Vittum, R.A., III; Khoda, B. Optimizing Beam Stiffness and Beam Modal Response with Variable Spacing and Extrusion (VaSE). *Designs* **2025**, *9*, 64. https://doi.org/10.3390/designs9030064

Copyright: © 2025 by the authors. Licensee MDPI, Basel, Switzerland. This article is an open access article distributed under the terms and conditions of the Creative Commons Attribution (CC BY) license (https://creativecommons.org/licenses/by/4.0/).

1. Introduction

Material extrusion (ME) based additive manufacturing (AM) is one of the most common forms of additive manufacturing due to its low cost and simplicity to use. A typical ME printer entails a heated nozzle that operates in three axes. The nozzle extrudes melted polymer layer by layer to create the designed part [1,2]. Parts created using ME are rarely solid; instead, infill, a repeating pattern generated using a Cura slicer software V5.9 program, is used to create an internal structure within the part to reduce its weight and the time to print. The percentage of infill relative to the total volume of the part, the type of pattern used, and the orientation of the infill pattern all affect the mechanical properties of the printed object [3–6].

A functionally graded infill structure varies spatially to optimize its performance under different loading conditions [7]. By changing the infill percentage, pattern, orientation,

and other properties of the infill in key areas, as opposed to maintaining homogeneity throughout the object, a printed part's mass can be distributed in a manner to maximize its performance in specific mechanical loading conditions. Such functionally graded structures have the same goals as topology optimization, which constitutes algorithms that determine the best use of distributed material for a part in such a way that, while reducing the weight of the structure, the stiffness indicators and the natural frequency of the structure are consistent with those in the catalogue of target indicators and limitations [8,9].

Using infill as a controllable porous planar structure makes it possible to create an ME-printed part that is functionally graded for specified loading conditions [10–22]. For instance, one study proposed a voxel-based method of constructing and skinning conformal and functionally graded structures suitable for additive manufacturing [18]. The method involves tessellation and trimming of unit cells to conform to any external geometry and can be extended to efficiently generate functionally graded lattice structures. Another work proposed a novel method for generating functionally graded cellular structures using error diffusion technique [19]. The method involved three main stages: defining functional grading, error diffusion to generate dithered points of the boundary and area, and applying a connection scheme to generate structure cells. They concluded that error diffusion is an efficient and novel way to create functionally graded cellular structures with a small number of design variables. The method proposed was able to generate structures with varying cell sizes and shapes. Similarly, another algorithm proposed a framework for stress-based lattice structure topology optimization for additive manufacturing [20]. An asymptotic homogenization method was used to obtain the effective elastic properties of the porous structure in terms of relative density, and a fourth order polynomial was proposed for the curve fitting along the density range. For the effective yield strength, the modified Hill's yield criterion considering multiple loading cases of a unit cell was applied to estimate the plastic performance of lattice structure. The proposed optimization framework for porous structure with periodic cell achieved superior performance on mechanical properties, such as stiffness, yield strength, ultimate strength, and energy absorption, compared to the uniform design. The proposed homogenized model coupled with the modified Hill's yield criterion provided a reasonably accurate representation for the performance of graded structure design. Such topology-optimized structures can generate lightweight designs achievable by additive manufacturing with predictable yield performance.

These proposed methods all have the limitation of requiring overly complex geometric models that most commercial slicing software programs and ME printers, specifically, struggle to produce. Geometric models, such as STL required to capture small thin features of a part, will greatly increase computational time because STL models read the part utilizing triangles as surface discretization. Polygon count of an STL, and thus accuracy, is proportional to slicer computation time by an order of n^2. The three-axis system in tandem with the layer-by-layer approach to printing limits the complexity of the part that can be made. While systems with greater degrees of freedom are being explored to overcome the setbacks of normal ME printers, such as the use of robotic arms, these innovations are still in development and have nowhere near the popularity of the well-known three-axis desktop printers used widely today [21]. The cartesian motion systems are well suited for linear interpolation and reduce the dimensionality of the polynomial path with piece-wise linear approximation. This reduction in dimensionality undermines the higher-degree discretization of the design domain that often results from the common topology optimization technique discussed earlier. Therefore, it is crucial to account for the constraints of the three-axis printers when designing and developing algorithms for ME additive manufacturing.

In an attempt to work with the ME manufacturing limitations while achieving the desired results of topology optimization and graded functional structures, some have proposed modifying or generating the infill structure for additive manufacturing at the machine parameters level, avoiding complex geometric modeling. For instance, one paper sought to modify the extrusion width of a gyroid lattice structure to achieve a functional grading without the need for complex geometrically defined models [22]. However, while it was proposed that the method could do so by modifying the machine parameters directly and avoiding geometric modeling, there is an inherent limit to the change in effective mechanical properties by changing extrusion width or the member size alone. To overcome this, the addition of local control of cell size was proposed to add further control of density within the design domain.

Recently, a functionally graded infill algorithm was proposed that allows for any density-based input to be post-processed and realized as lattice, inherently ensuring manufacturability and avoiding any complex geometric modeling by creating an infill structure directly as machine parameters [23]. The previous work sought to demonstrate that the proposed infill generation algorithm, expanded upon in the methodology section of this paper, can generate machine parameters that reasonably reproduce an arbitrary density distribution in the form of an ME-printed object. The algorithm herein will be called Variable Spacing and Extrusion (VaSE), which also ensured manufacturability. During the experiment, various density distributions were manufactured using a variable line spacing and variable extrusion width algorithm with known centers of gravity. The accuracy of VaSE was evaluated by quantifying the deviation in the center of gravity between the designed and manufactured structures.

The work herein aims to further apply this algorthm to the following two density-based topology optimization scenarios: maximizing the flexural stiffness of a beam under a three-point load and maximizing the frequency of the first three modal responses of a vibrating cantilevered beam. The goal of this paper is to show that the VaSE algorithm can create objects that are matched or superior in performance to other methods for specific loading cases. For instance, during the flexural stiffness testing, the VaSE is compared against the basic homogeneous infill created by Cura. In the modal response testing, the VaSE is compared against a topology optimization algorithm whose final geometry is directly extracted and printed.

2. Materials and Methods

2.1. Methodology Behind the VaSE Algorithm

The proposed VaSE algorithm consists of two algorithms, namely (i) variable line spacing (VLS) and (ii) variable extrusion width (VEW). The following explains the theory and workflows behind the VaSE algorithm seen in [23,24].

2.1.1. Creating a Toolpath to Obtain the Variable Line Spacing (VLS)

Any density-based input can be utilized with this algorithm. However, such inputs need to be normalized to implement the VaSE algorithm. For example, the input for the algorithm can be a color map nodal value input from finite element analysis or an image (e.g., gray scale or RGB), where the value of the pixel can be mapped as the relative density value. The mapping between pixels and densities can be performed with experimental values or using a continuous function such as the power law [13,25]. Such a discretization is coherent with the current discrete element analysis tools and simplifies the process of finding density averages by eliminating the need for any calculus but at the cost of potentially reduced accuracy. However, using a continuous distribution may not be necessary due to the manufacturability constraints requiring deposition-level discretization in the

3D-printing process. Instead, a discretized version of a distribution is just as useful, and, if it is in the interest of the user of the algorithm, a convergence study could be performed to see where the solution seems to have no change as the number of discrete points is increased. To initialize the VaSE algorithm, we used a very fine discretization that is much smaller than the resolution of the printing (diameter of the filament or minimal line spacing width) to capture the accuracy of the output as much as possible. In the previous work, a continuous density distribution, based on a simple second-degree polynomial equation, was discretized over a domain [23].

Rectilinear infill is used in this algorithm for its simplicity and demonstration purpose. Since this infill type creates a grid along only one axis per layer, an additional pre-processing step must be performed, where the discretized graded density can be transformed into two vectors for bilayer: a vector representing the mean element value perpendicular to the raster angle of the arbitrary m-th layer and another representing the mean element value perpendicular to the raster angle of the m + 1 layer. An example of this process for a layer with a raster angle parallel to the y-axis, i.e., the working axis is y, is shown in Figure 1.

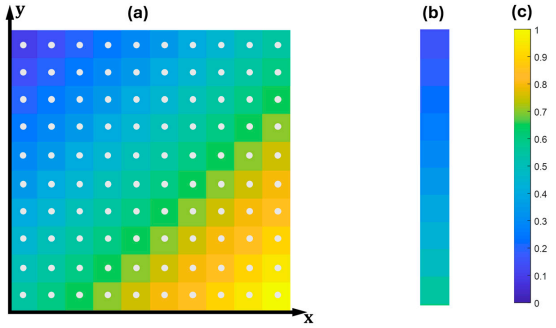


Figure 1. Preprocessing density into a vector, ρ_{layer}, for a single layer, working in the y axis, where (**a**) is the discretized density distribution, (**b**) is the average density for each row of the distribution, and (**c**) is the color bar ranging from 0 to 1, indicating the local density of the distribution.

Only the array, ρ_{layer}, corresponding to the working axis of the layer is needed to determine line spacing, as shown in Figure 1. The desired line spacing for a given density is calculated as

$$L_{spacing} = \frac{w_{extrusion}}{\rho} \tag{1}$$

where ρ is the desired relative density, $w_{extrusion}$ is the nominal extrusion width in millimeters, and $L_{spacing}$ is the spacing between the extrusion lines, i.e., the toolpath. To further reduce computation time, Equation (2) can be applied during preprocessing to convert the array of densities, ρ_{layer}, into an array of corresponding line spacing, as follows:

$$u = \frac{w_{extrusion}}{\rho_{layer}} \tag{2}$$

where u is a vector of the desired spacing for each layer, or, rather, for each averaged row as seen in Figure 1. This preprocessing eliminates the need to apply this function at each iteration across the whole discretized density distribution in the process of determining the overall optimum line spacing. This allows for decreased processing time. Finding the line spacing at a given point is best defined as an optimization problem, where the objective function is to minimize error between the average enclosed density value and the given line spacing, which can be expressed as the following:

$$min\ error_i = \left(u_{avg,enclosed} - L_{spacing}\right) \tag{3}$$

s.t.

$$w_{extrusion} < L_{spacing} < L_{Max}$$

where $u_{avg,enclosed}$ is the average enclosed density value. The average enclosed density value is calculated as

$$u_{avg,enclosed} = \frac{\sum_{n=i}^{L_{spacing}} u_n}{L_{spacing}} \quad (4)$$

where u_n is the nth term in the desired spacing vector, and i is the index representing the start of the enclosed region. The index i denotes the element at the position of the previous extrusion line, except for when finding the first spacing in which it is initialized equal to 1. The workflow for the variable line spacing algorithm utilizing bisection search for determining the optimum line spacing for a layer is shown in Figure 2. A bisection search method is employed to solve the minimization problem for each line spacing in series because the problem is reduced into one dimension. The goal of bisection search is to find the root of a function given two numbers of a function, where A is the minimum spacing, C is the maximum spacing, and B is halfway between A and C.

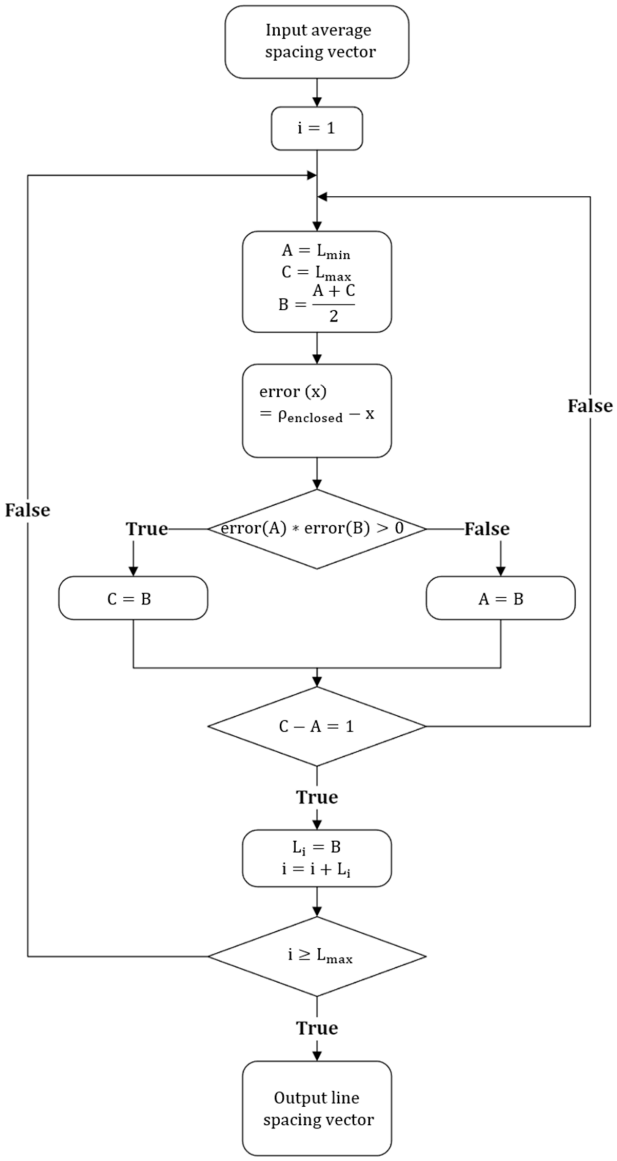


Figure 2. VLS algorithm using bisection search for determining the line spacing and toolpath.

After each optimum spacing is found when the bisection search converges, the index i is incremented by L_i such that i is now the starting position of the next line spacing. When i is equal to the length of the array, u, the spacing of the extrusion lines has been determined for the whole domain, and the loop ends. The output is an array, L, that contains the spacing in sequence and, therefore, the position of the extrusion lines across the domain. Using this array, the toolpath is created by simply adding the moves between lines. An example of optimized toolpaths is shown in Figure 3. It can be observed that in the higher-density regions in Figure 3a, there is a corresponding tighter line spacing observed from the workflow in Figure 3b and vice-versa for low density regions.

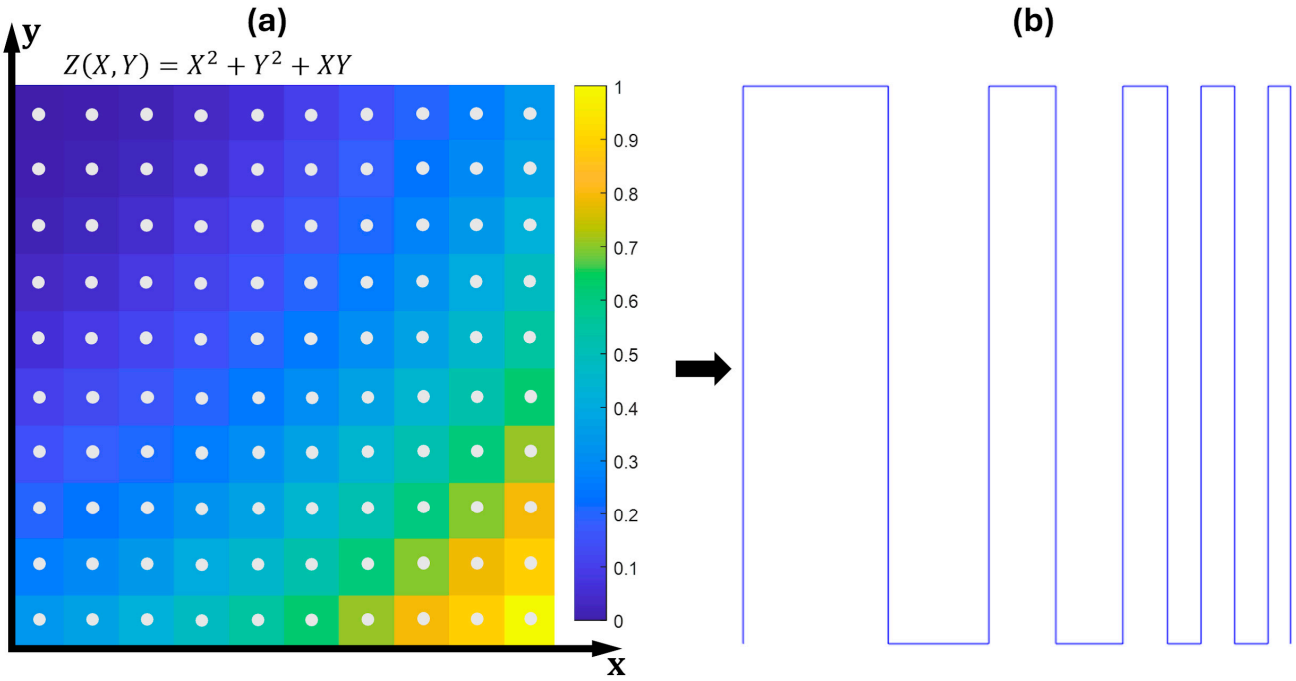


Figure 3. An example showing (**a**) a discretized density distributions and (**b**) its corresponding line spacing from the VLS algorithm.

2.1.2. Determining the Variable Extrusion Width (VEW)

Since the line spacing algorithm is reducing the dimensionality of the 2D pixel distribution into 1D line spacing, the method will generate an error distribution. To compensate, variable extrusion width is proposed using the error from the variable line spacing toolpath. From the toolpath created for the variable line spacing, a matrix representing the homogenized relative density can be constructed. The matrix is used along with the discretized input density matrix to calculate the error in the relative density as

$$[\rho_{error}] = [\rho_{input}] - [\rho_{VLS}] \tag{5}$$

where matrix ρ_{error} represents the discretized error in density, calculated as the difference between the input desired relative density matrix ρ_{input} and the relative density matrix ρ_{VLS} of the toolpath generated by the VLS step of the algorithm. To best portray this, an example of ρ_{VS} and ρ_{error} is shown in Figure 4 based on the graded density presented in Figure 1.

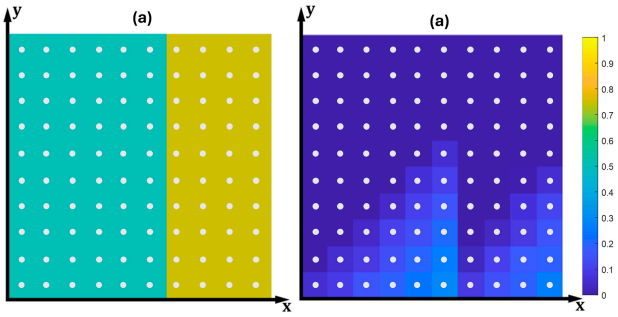


Figure 4. (**a**) Relative density of the toolpath, ρ_{VS}, and (**b**) percent error between ρ_{error} and ρ_{input}.

As both relative density matrices are already normalized, the resulting matrix, ρ_{error}, consists of the signed percent error for each element and is used to generate a matrix of extrusion width variation. The extrusion width variation is calculated by simply subtracting the matrix, ρ_{error}, from an identity matrix to find yet another new matrix, called W, that contains the desired extrusion width as a percentage of the nominal extrusion width. The equation for W is as follows:

$$W = I - \rho_{error} \tag{6}$$

where I is the identity matrix. The error matrix is used to determine the extrusion width variation that will reduce the error of the optimum toolpath by locally changing the filament diameter. To this end, the matrix W needs to be further process to determine the optimum extrusion width along each line of the toolpath by averaging the element desired width within the region around it. To determine the extrusion width for a given line i, the region halfway to the line before and after is taken as the area of influence for line i, as shown in Figure 5.

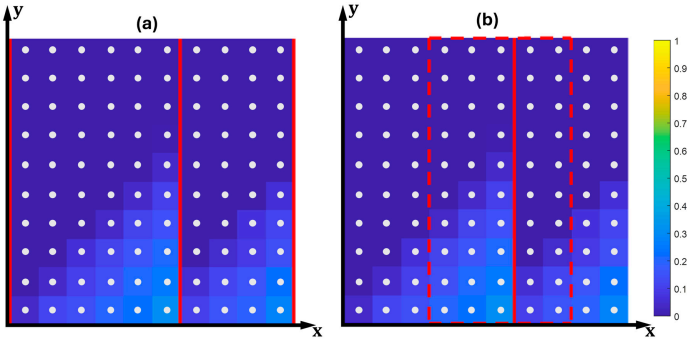


Figure 5. (**a**) Error with extrusion line $i-1$, i, and $i+1$ overlayed in red, (**b**) the area of influence for line i bounded by the red dotted line.

For the example presented in Figure 5, this area of influence for line i can be defined as

$$W_L = W[1,10; a=3, b=8] = \begin{bmatrix} 1.25 & 1.20 & 1.15 & 1.35 & 1.29 \\ 1.19 & 1.15 & 1.10 & 1.29 & 1.25 \\ 1.15 & 1.11 & 1.05 & 1.24 & 1.19 \\ 1.11 & 1.04 & 1 & 1.19 & 1.14 \\ 1.04 & 1 & 0.96 & 1.16 & 1.09 \\ 1 & 0.95 & 0.90 & 1.11 & 1.04 \\ 0.96 & 0.89 & 0.85 & 1.05 & 1.01 \\ 0.89 & 0.84 & 0.79 & 1 & 0.95 \\ 0.86 & 0.79 & 0.75 & 0.94 & 0.88 \\ 0.80 & 0.77 & 0.69 & 0.90 & 0.85 \end{bmatrix} \tag{7}$$

where a is the index of the element halfway between line $i-1$ and line i, and b is the index of the element halfway between line i and line $i+1$. The matrix, W_L, representing the area of influence, is then averaged perpendicular to the line creating a vector representing the optimum extrusion width for line i. An extrusion line parallel to the y-axis, $\vec{w}_L$, can be found for Figure 5 as follows:

$$\vec{w}_L = \left(\frac{\sum_{m=a}^{b} W_L[n;m]}{b-a} \right)_n = [1.25\ 1.20\ 1.15\ 1.10\ 1.05\ 1.00\ 0.95\ 0.89\ 0.84\ 0.80] \quad (8)$$

Finally, $\vec{w}_L$ can then be multiplied by the nominal extrusion width (typically 0.4 mm for most ME 3D printers) to calculate an array of the desired extrusion width in millimeters, w_{ext}. The array for desired extrusion width can be found using the following:

$$w_{ext} = 0.4\ \vec{w}_L = [0.50\ 0.48\ 0.46\ 0.44\ 0.42\ 0.40\ 0.38\ 0.36\ 0.34\ 0.32\ ] \quad (9)$$

Once w_{ext} has been determined for each extrusion line, the toolpath and extrusion width information can be utilized to generate the machine parameters.

2.1.3. Piecing Together the Variable Line Spacing (VLS) and Variable Extrusion Width (VEW) to Create Usable Machine Parameters Commands for an ME Printer

A custom machine parameters generation/slicer script was written in MATLAB to handle slicing. The script takes the extrusion line spacing and width data as arrays generated by the VaSE method as input. The arrays are preprocessed and binned by extrusion width, creating the longest possible line segments per machine parameters line to help reduce the total number of lines. Without this preprocessing, the number of lines of machine parameters would quickly grow. The algorithm for this preprocessing is shown in Algorithm 1. This would result in the file size proportionally increasing with the size of the elements.

Algorithm 1 Generation of Machine Parameters

```
for j := 1 to Number of lines do
    Break up extrusion lines by similar E-vale
    i = 1;
    P1 = 1;
    P2 = 2;
    while P2 do
        while ExtModX_{P1,j} do
            P2 = P2 + 1
        end while
        subline(i,:) = [P2, P2 − P1, ExtModX_{P1,j}];
        P1 = P2;
        i = i + 1
    end while
    Generate x, y, and E data
end for
End procedure
```

The slicer script is basic in its computation of the extrusion value, E, the rotation for the extruder stepper to advance, which is given as

$$E_{value} = \frac{4A_{ext}L_{ext}}{\pi d_{filament}} \tag{10}$$

where A_{ext} is the cross-sectional area of the extrusion, L_{ext} is the length of the path, and $d_{filament}$ is the diameter of the filament. The extrusion multiplier is recalculated from the Cura software for its standard printing. During the extrusion control, the extrusion multiplier is determined using linear interpolation.

In this work, the filament cross section is assumed to be a filleted rectangle in shape, as shown in Figure 6, and it is calculated as

$$A_{ext} = hw_{ext} - h^2 + \frac{\pi}{4}h^2 \tag{11}$$

where h is the layer height and w_{ext} is the extrusion width in millimeters. Implementing some of the advanced methods used to compensate for such limitations in commercial slicers could greatly improve the performance of the VaSE method, but attempting to integrate the commercial slicers was deemed unnecessary to show the validity and capabilities of the VaSE algorithm.

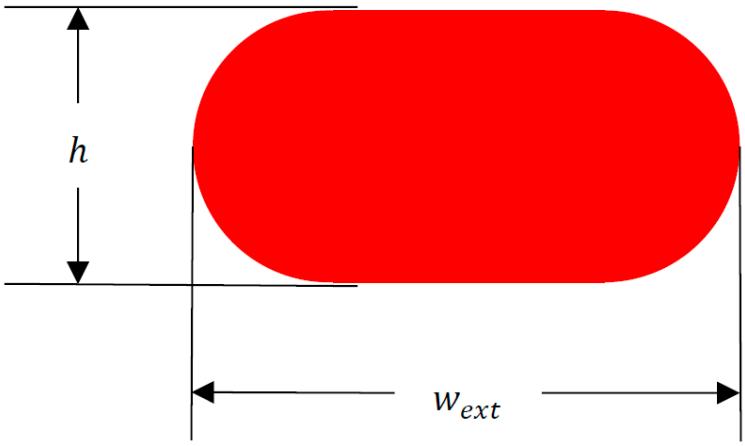


Figure 6. Ideal cross section of an extrusion line.

3. Optimizing Beam Stiffness with the VaSE Algorithm

The VaSE algorithm was utilized to manufacture beams that are far stiffer when compared to beams manufactured with a homogenous infill of the same density. To measure this increase in stiffness, the effective flexural elastic modulus was measured based on the ASTM standard (#D790-17) for measuring flexural properties of plastics and electrical insulating materials. It is a version of a 3-point bending test. Using rectilinear infill for simplicity, beams with 25%, 50%, and 75% infill were used for the experiment. The beams' dimensions were selected as 250 mm × 12 mm × 12 mm to be long enough to prevent slippage through the fixture and to have sufficient width and height, with a desired span-to-depth ratio of 16:1. For the beams with optimum stiffness, the well-known "99-line Topology Optimization" MATLAB script [26] was used, with slight modifications to extract the optimized density distribution of the beams and enter them into the VaSE algorithm. The machine parameters of the specimens were generated after running through the VaSE script, which can be seen in Figure 7, using Ultimaker Cura to visualize the beams. A close-up of the VaSE parts in Cura is shown in Figure 8 to clearly display the varying extrusion width of the beads over the parts.

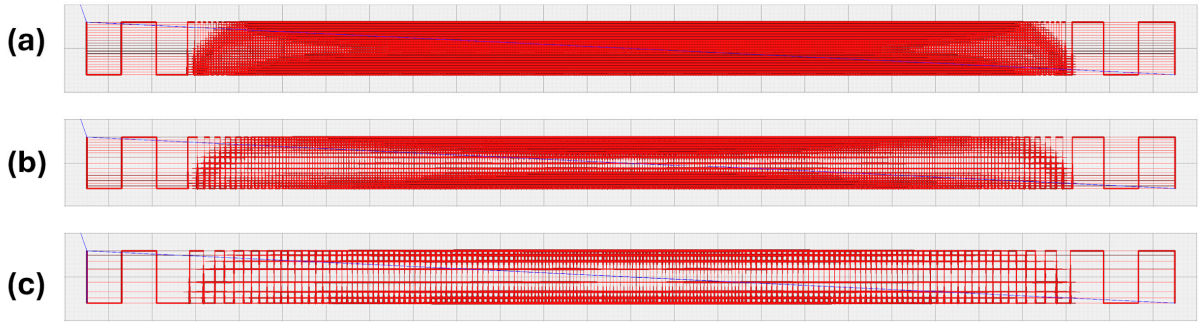


Figure 7. Cura visualization of the beam machine parameters generated after applying VaSE algorithm: (**a**) 75%, (**b**) 50%, and (**c**) 25% infill (blue lines are the non-deposition motion).

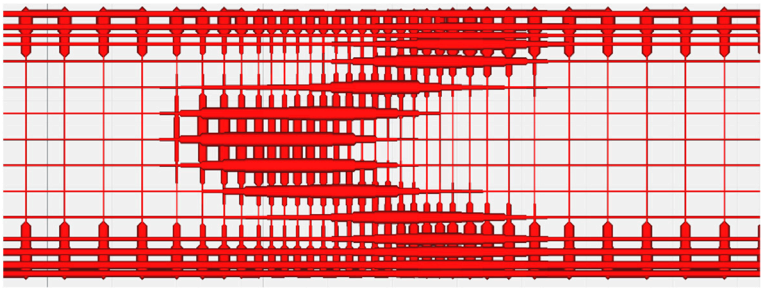


Figure 8. A sample close-up of the varying extrusion width of a VaSE part is depicted from Cura visualization.

For the homogeneous control specimens, the machine parameters were created by entering the STL file of the beams into the commonly used Cura slicer software V5.9 and slicing the beams with the specified (25%, 50%, and 75%) infill percentage, a rectilinear infill pattern, and no outer walls. The Cura visualization of the beams can be seen in Figure 9.

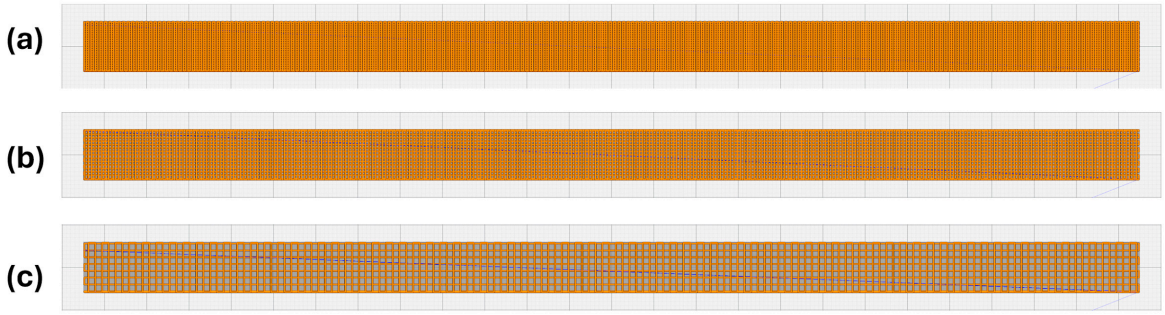


Figure 9. Visualization for the homogeneous infill beams as control (**a**) 75%, (**b**) 50%, and (**c**) 25% infill (blue lines are the non-deposition motion).

All the beams were printed on an Ultimaker S5 with Ultimaker ABS filament because the higher compliance of the ABS would better highlight any improvements in beam stiffness as opposed to the more commonly used PLA [27]. A standard 0.4 mm nozzle was used, and each layer of each beam was printed with a height of 0.2 mm. All other parameters were set to Cura's default values and remained the same for both beam sets. The ASTM D790-17 standard indicates that the strain should not exceed 5% while testing. The approximate maximum deflection, D, was determined in accordance with this 5% maximum strain using the equation:

$$D = \frac{rL^2}{6d} \tag{12}$$

where r is the strain, L is the support span of the beam, and d is the depth or thickness of the beam. The specimens were oriented such that the load and supports were in-plane with the print layers. The variable density specimens were marked to indicate the support and load faces to ensure proper orientation.

4. Optimizing Beam Modal Response Utilizing the VaSE Algorithm

For this experiment, a cantilever beam was optimized with the goal of maximizing the frequency of the modal response and the constraint of optimized mass relative to the original beam. Just like the beams used for optimum stiffness, the beams designed for modal response had dimensions of 250 mm × 12 mm × 12 mm. Twenty millimeters of one end of the beam was clamped down, while the other was left free to model a cantilevered beam setup. The optimization algorithms were performed in ANSYS as a density-based topology optimization utilizing the SIMP method. The penalization factor, also known as stiffness, was kept at the default value of 3. The beam was modeled as a shell model with a square cross section of 12 mm in size. For meshing, 4-node quadrilateral elements were utilized with an element size of 1 mm. A mass constraint was placed on the optimization region. Three different mass constraints were used to create three different beam designs of varying relative densities to be analyzed as might be done for a typical optimization design study. The optimization region was set to exclude the 20 mm clamped support region as well as the perimeter of the beam, preserving the external shape as would possibly be desired from a beam, as seen in Figure 10. The topology optimization created a field of the optimum relative density distribution per node.



Figure 10. Mass constraint of the beams optimized for modal analysis, where red boundary indicates the area of mass to be excluded and only blue area is used for the topology optimization.

These resulting nodal relative densities were then post-processed using the VaSE infill algorithm and the traditional geometry extraction method. The geometry extraction postprocessing of the topology optimization results was handled within ANSYS, and the workflow is shown in Figure 11. In the first step, the elements of the optimized density distribution that were below the threshold of 50% mass fraction were removed, and the remainder were assumed to be solid. This resulted in a geometry with a jagged boundary. As such, ANSYS utilized a skewness-based method for smoothing these boundaries. Finally, the extracted geometry was exported as an STL file, and the machine parameters were generated using the Ultimaker Cura slicer software, seen in Figure 12.

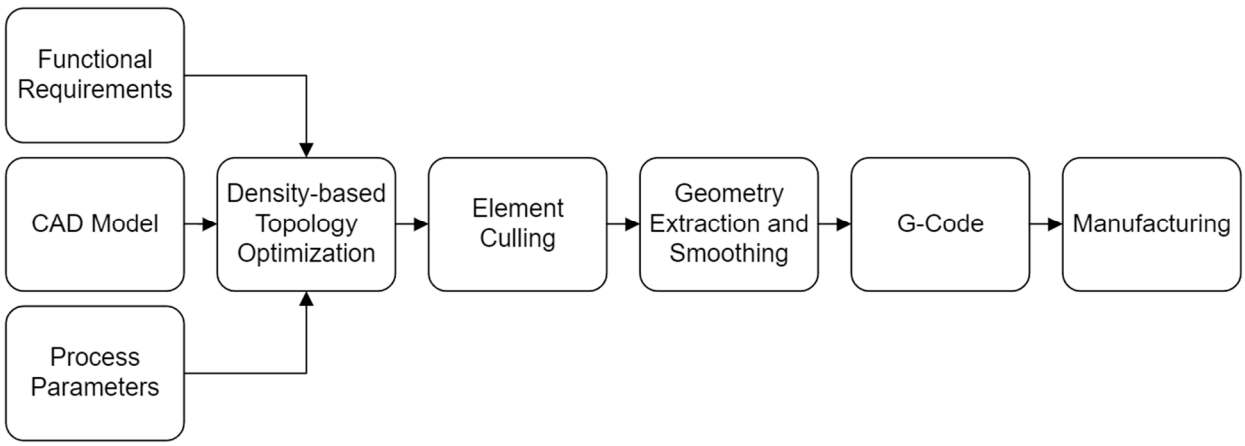


Figure 11. Workflow for the geometry-extracted optimized beams from ANSYS for modal analysis.



Figure 12. Visualization of geometry-extracted beams optimized by ANSYS for mass fractions of (**a**) 82%, (**b**) 61%, and (**c**) 40% (red color represent the contour boundary of the void; yellow a nd green are the infill).

The workflow for the VaSE algorithm optimized infill method is presented in Figure 13. To start the postprocessing of the results using the VaSE infill method, ANSYS was used to export a simple text file to indicate nodal locations of the beam and the respective density value at those nodes.

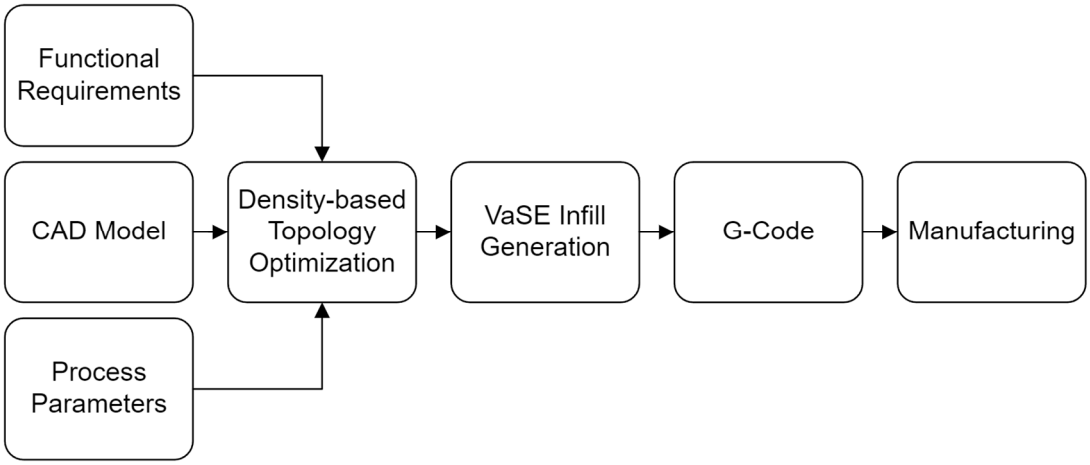


Figure 13. Workflow of the VaSE-optimized beams for modal analysis.

The text file was imported into MATLAB, creating a matrix of the desired density distribution. The VaSE algorithm could be applied to this matrix, generating machine parameters for the functionally graded lattice structure to be manufactured, visualized in Figure 14.

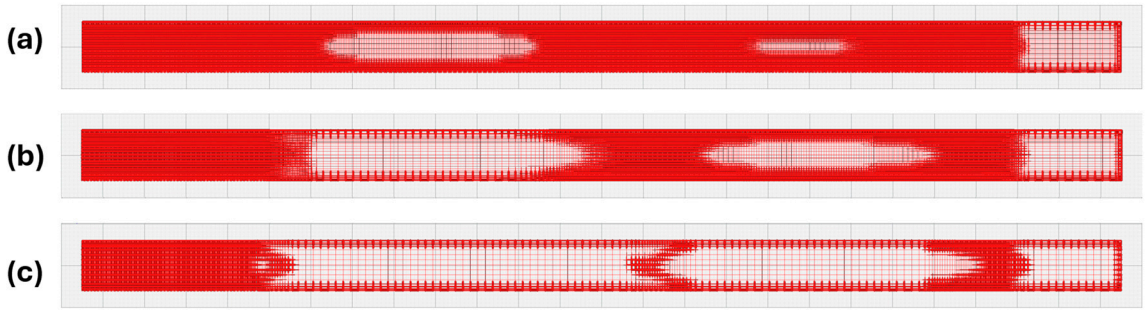


Figure 14. Visualization of VaSE-optimized beams with mass fractions of (**a**) 82%, (**b**) 61%, and (**c**) 40% (blue lines are the non-deposition motion).

All specimens were printed on the Ultimaker S5 using Ultimaker ABS. A standard 0.4 mm nozzle was used, with a nominal extrusion width of 0.4 mm and a layer height of

0.2 mm. Figure 15 shows the test setup for the modal analysis. A 20 mm length of the solid end of each beam was clamped between steel plates. A PCB Piezotronics model 333B32 accelerometer was adhered approximately 1 mm away from the top clamping plate using PCB Petro wax. The accelerometer signal was collected using a National Instruments cDaq system, consisting of an NI 9234 acceleration module in a cDaq 9171 chassis. NI DAQ Express software (2024 Q1) was used to collect data at a sampling rate of 25,600 Hz. The collected data for each run were imported into MATLAB R2021a software. The MATLAB "fft" function was used to compute the discrete Fourier transform of the data. The mode frequencies were determined from a plot of the transform. The tests were performed using the step relaxation technique, which is a method where the end of a beam is deflected approximately 10 mm and released, inducing vibration.

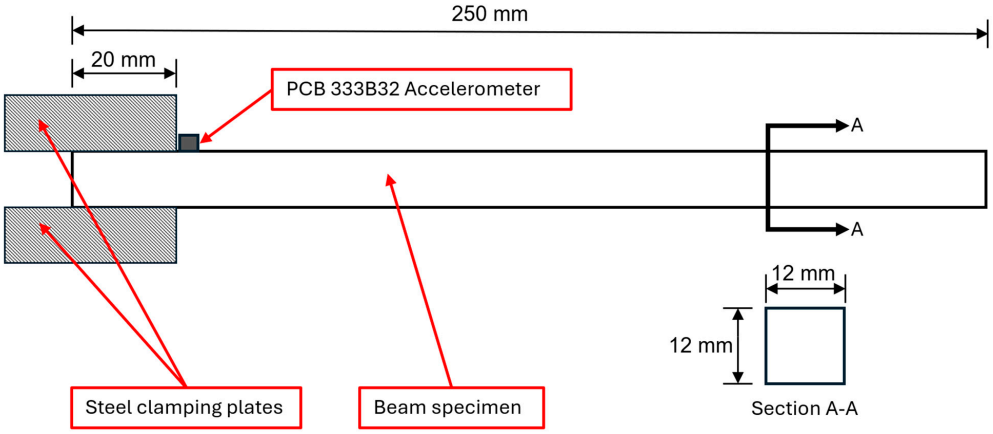


Figure 15. Test setup for beam vibration during modal analysis experimentation.

5. Results and Discussion

5.1. Beam Stiffness

While all samples printed satisfactorily, as seen in Figure 16, there were some differences in the printed specimens from the visualization of the machine parameters in Cura. This is partially due to the "elephant foot" effect, where the first layer is more spread out, making it harder to see through the part. Additionally, the extrusion lines were circular in their cross section when not directly supported by the layer beneath, as opposed to the roughly rectangular cross section assumed by the visualization; the bead maintained this shape because nothing was compressing it after it was extruded from the nozzle.

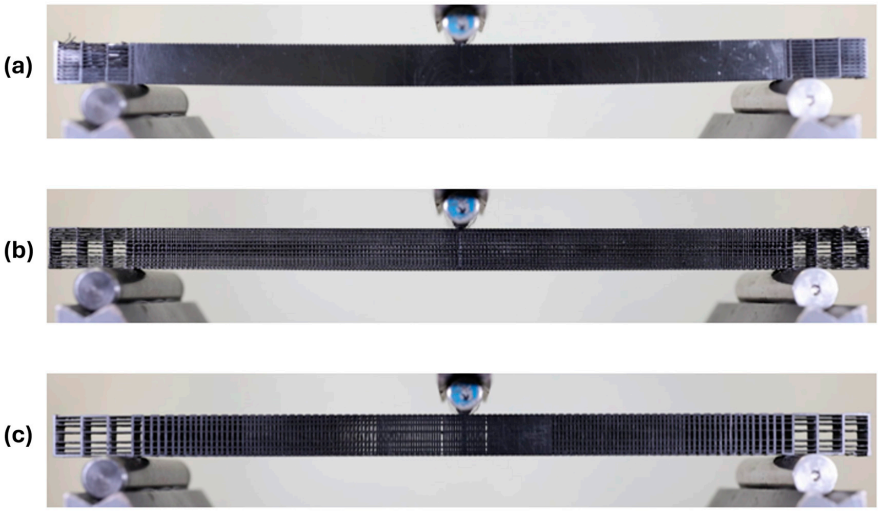


Figure 16. Optimized beams with (**a**) 75% infill, (**b**) 50% infill, and (**c**) 25% infill.

The stress–strain graphs for the experimental tests are presented in Figure 17. The effective flexural elastic modulus was calculated as the slope of the linear region for each. To ensure yielding and no linear effect where not captured, this linear region was taken to be from 0.005 to 0.01 strain.

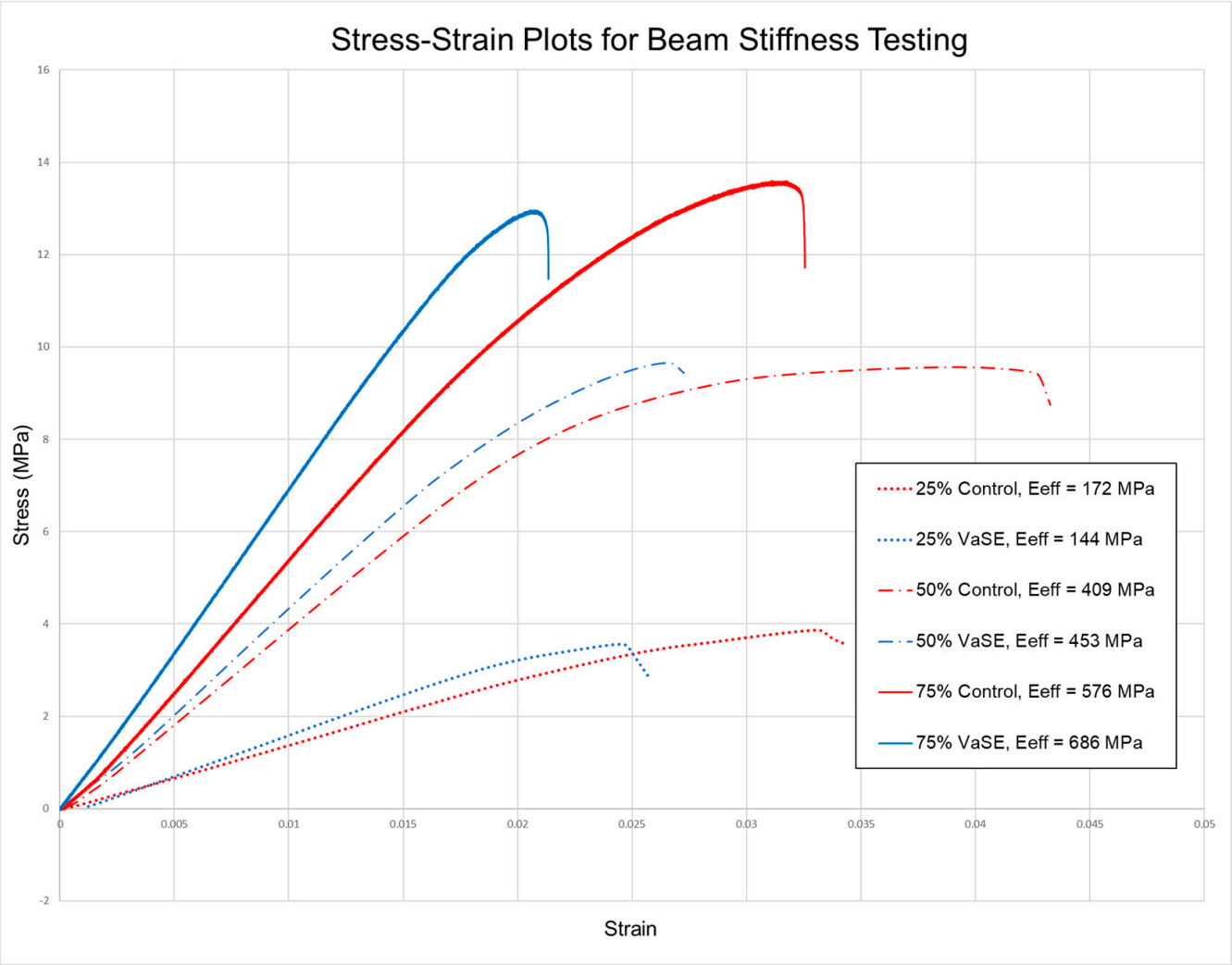


Figure 17. Stress–strain plots for beam stiffness testing.

The 50% and 75% infill beams performed as expected. The 50% VaSE infill specimen showed a 10.8% increase in the effective flexural elastic modulus over the homogenous 50% rectilinear infill samples. For the 75% VaSE infill specimen, an even greater improvement in the effective flexural modulus was observed, at 19.2% improvement over the 75% homogenous infill specimen. The 50% and 75% infill specimen failed in tension along the underside of the beam opposite the load head. This is the same failure mode that would be expected of bulk, injection-molded ABS. The 25% infill specimens, both control and optimized, experienced local buckling. In the optimized 25% specimen, buckling could be observed at much lower loads, indicative of the lower effective stiffness observed. In these optimized specimens, out-of-plane bulking, seen in Figure 18, was prominent in the regions with a line spacing in the vertical axis corresponding to less than 10% infill. It is important to note that this behavior was not seen in the corresponding control specimens.

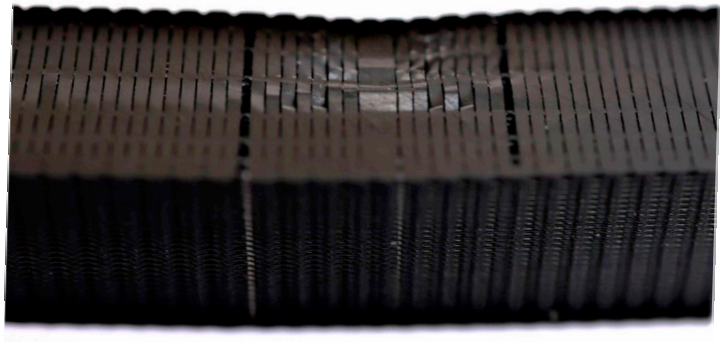


Figure 18. Local buckling observed with the 25% infill beam, created with the VaSE algorithm.

The assumption that the material was isotropic was invalid even when conditions for the other assumption were met. This is due to the geometry of a lattice structure, which would more accurately be modeled as anisotropic. The VaSE algorithm introduces further anisotropic behavior, as it allows for a change in the aspect ratio of the lattice unit cells. This was particularly apparent in the shear effects seen in the VaSE 25% beam during testing. Importantly, the solid material model utilized in the SIMP method, like most RVE models, cannot capture local bulking of the lattice cell members in the approximated material behavior. Thus, the predicted behavior may not be accurate if the actual geometry of the lattice structure would fail in local buckling.

5.2. Modal Response

Some difficulty was encountered when creating the geometrically optimized beams. When exporting the STL from ANSYS, the mesh was not manifolded due to mismatched surface normal vectors. Consequently, each STL file had to be repaired in Rhino3D before generating the machine parameters to manufacture the samples, which can be seen in Figure 19. This is an example of one of the issues in modeling that the VaSE infill algorithm can overcome.

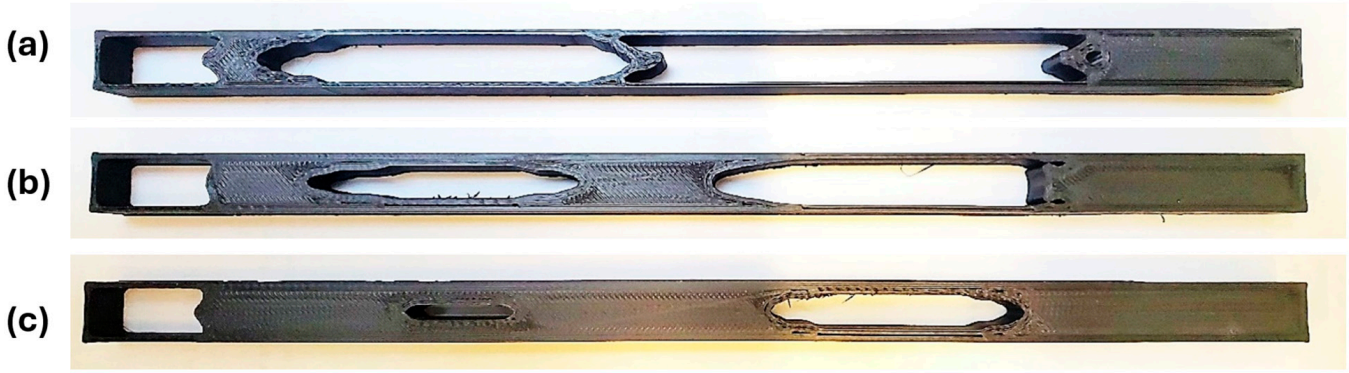


Figure 19. Geometrically extracted optimized beams with (**a**) 25%, (**b**) 50%, and (**c**) 75% infill.

Just like with the beams tested for flexural stiffness, the printed VaSE infill beams, seen in Figure 20, do not visually show the expected extrusion width modifications that they were designed for. Exactly like the flexural stiffness beams, the disagreements between the designed and manufactured parts were due to simple G-Code, "elephant foot" effects, large overhangs, and inadequate control of the printer to extrude the correct amount of material at the correct location.

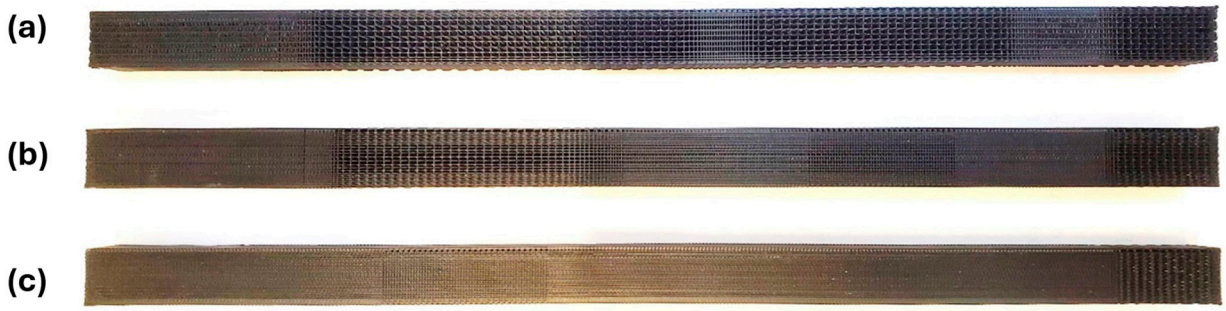


Figure 20. VaSE optimized beams with (**a**) 40%, (**b**) 61%, and (**c**) 82% infill.

After the beam vibration experiment, it was found that the first mode frequency had a tenuous agreement between the ANSYS predicted values and the experimental results of both methods. The higher mass fraction designs tended to better match the prediction. The extracted geometry samples performed particularly poorly for this mode, as can be seen in Figure 21. For the 40% mass fraction design, the sample at 14.8 Hz was 73% lower than the predicted 54.9 Hz. This was also 63% lower than the VaSE infill algorithm sample at 40.2 Hz. In contrast, the VaSE 40% sample was only 27% lower than the prediction. A similar trend could be seen for the 61% mass fraction design, with the VaSE infill algorithm sample again having a frequency of about 1.5 times that of the extracted geometry, with a decrease in deviation from the prediction. Finally, for the 82% mass fraction design, the VaSE infill algorithm did perform slightly worse than the extracted geometry, at 43.4 Hz and 48.8 Hz, respectively.

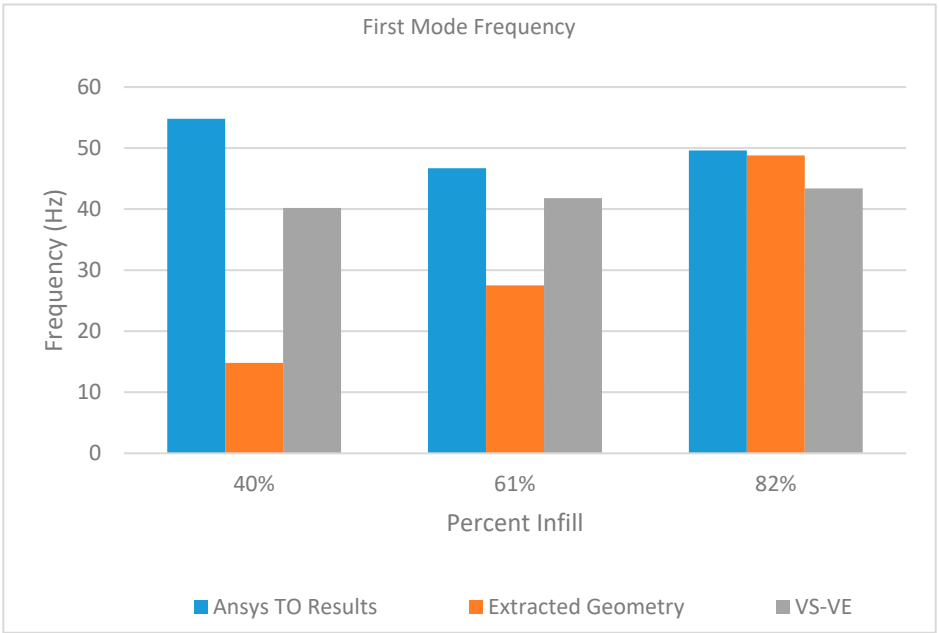


Figure 21. Results from the first mode frequency analysis.

The second mode frequencies had a correlation between the ANSYS predicted values and the experimental results of both methods similar to that of the first mode. The results can be seen in Figure 22. Higher mass fraction designs tended to better match the prediction, and the extracted geometry samples performed poorly for this mode. For the 40% mass fraction design, the shape-based sample at 68 Hz was 81% lower than the prediction and 65% lower than the VaSE infill algorithm sample. In contrast, the VaSE 40% sample was only 47% lower than the prediction. A similar trend could be seen for the 61% mass fraction design, where the VaSE infill algorithm had a frequency of about double that of

the extracted geometry, with a decrease in deviation from the prediction. Finally, for the 82% mass fraction design, the VaSE infill algorithm and extracted geometry samples had practically identical second mode frequencies.

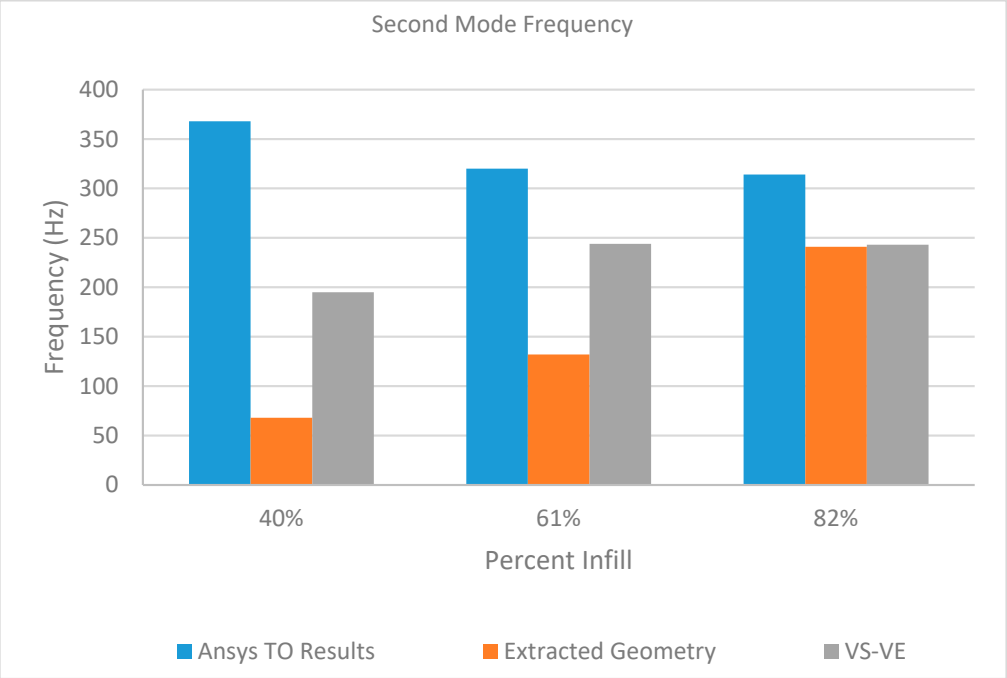


Figure 22. Results from the second mode frequency analysis.

As for the frequency of the third mode, while the validation of the experimental setup showed no issues with sensitivity, it could not be determined with any certainty across all samples in the experimental tests. The validation study of the extracted geometry predicted values for designs 1, 2, and 3 of 1040 Hz, 1030 Hz, and 918 Hz, respectively. The magnitude of this mode is believed to have been too small relative to the first two to be seen in the data. Figure 23 shows an example of the experimental results for the design 3 VaSE test beam in the frequency domain. No discernable peak was observed in the region of the expected 990 Hz predicted by ANSYS. As such, no results could be obtained for the third mode regarding the relative performance of either method utilized.

Upon analysis, the relationship between frequency and mass fraction predicted by the ANSYS results was not linear but rather seemed to be inverse. This trend was particularly noticeable for mode two. The ANSYS prediction differed greatly from the very clear proportional trend seen in the experimental measurements, for both the extracted geometry and VaSE infill beams, where frequency increased as mass fraction increased. One theory for this occurrence is that a change in mode shape may be predicted incorrectly by the solid homogenized model used by the optimizer. This may also help explain the vast difference in the frequencies predicted by the optimizer and the experimental results. Topology optimization is inherently a non-convex problem implying some dependency on the initial design. A validation study was conducted by setting beams to be a pre-set volume fraction before running the optimization. Comparing the predicted frequencies from each initial mass fraction, it had little effect on the design with a maximum deviation of 2.12%.

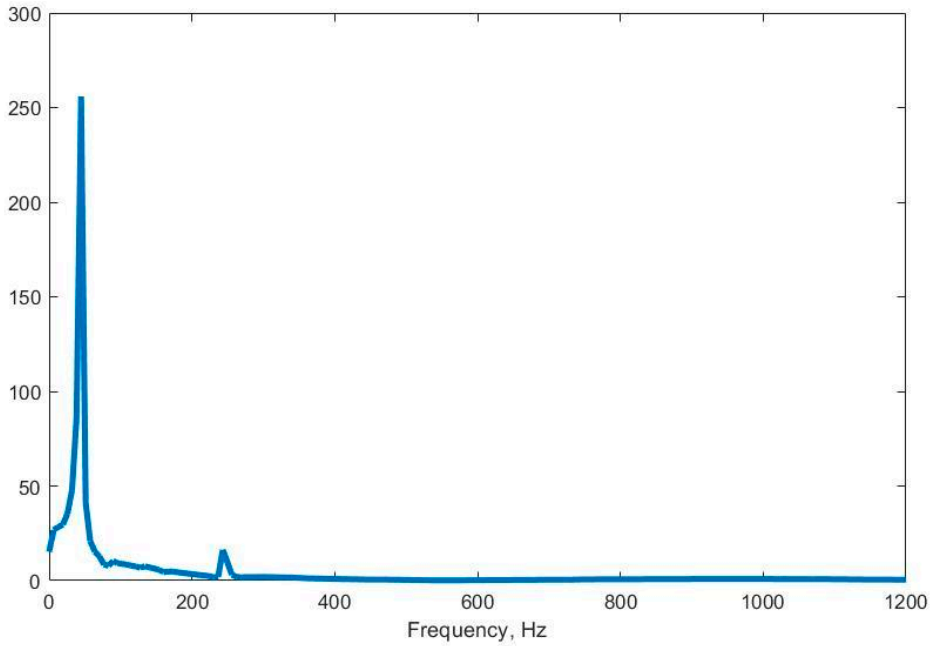


Figure 23. FFT graph results for the 82% VaSE infill sample.

It is important to note that while the frequencies were practically the same, the final geometry of the design did not vary with the initial mass fraction, and that there was no unique solution for this problem definition. This lack of dependency between predicted frequencies and initial design suggests the discrepancy in the frequency predicted by the optimization and the experimental results is not caused by an ill-defined initial design. By default, ANSYS uses the Block Lanczos method when performing a modal analysis, and the topology optimization utilizes the exact same solver parameters as the modal system defined beforehand. The same is true when running a validation study of an extracted optimized geometry. As such, it is expected that the choice of eigen-solver should not have an appreciable effect on the difference in the predicted mode frequencies or account for the odd trend. To confirm this idea, the same optimization was performed with three different eigen-solvers available within ANSYS for this setup: Block Lanczos, SCP Lanczos, and Supernode. No variation in optimized geometry was observed among these solvers. Therefore, the eigen-solver used had no appreciable effect, if at all, on the predicted frequencies, and it also has no appreciable effect on the observed inverse trend between mass fraction and frequency.

The variational deposition width in the printed parts was not obvious as designed in the algorithm. Little change in bead width could be observed in the parts, especially in critical areas where such behavior should have been obvious. However, the total mass of each printed part was exactly as expected, suggesting that the correct amount of material was deposited and that this was just a visual difference. As material-extrusion printers are mostly extrusion-rate limited, it also makes sense that we observed approximately equivalent print times for the VaSE specimens compared to their corresponding control samples. Therefore, we propose that the printer is attempting to follow the inputs and vary the bead width; however, due to the simple G-Code used, the lack of controls utilized to create the variable extrusion width behavior in adequate time, and the fact that the printers used have a Bowden tube for the extruder system, there were large delays that prevented the corrected material from being deposited in the correct location. Additionally, a control system with adequate response time, such as that seen in [28,29], can be a possible solution to have adequate control of the deposition width control, and thus, be able to vary the extrusion width at the desired amount. The two objectives were analyzed separately

to show the ability of the algorithm to be implemented in multiple scenarios, creating a better output than the nominal output of topology optimization or uniform samples. Certainly, a multi-objective approach could be analyzed in future work. We adhered closely to standard design, manufacturing, and testing protocols in reporting our findings; however, no statistical significance is presented due to time and resource constraints, which represents a potential limitation of the study.

6. Conclusions

In this work, a VaSE algorithm suitable for extrusion-based 3D-printing is proposed. The algorithm considered both filament spacing and extruded material volume to determine the deposition plan for performance better than that of the corresponding control specimens. Two experiments were performed to evaluate the effectiveness of the proposed VaSE infill algorithm. In the first experiment, beams were optimized for flexural stiffness based on the desired mass fraction and placed under a simply supported 3-point bending load. They were then compared to a homogenous infill beam of the same relative density. For most cases, the VaSE algorithm produced beams that were stiffer, except for the beams with a local density below 10% in which a buckling failure mode occurred. As the topology optimization that generated the density distribution did not have a local buckling constraint imposed, it was concluded that the reduced stiffness is attributed to the limitations of the optimization problem definition and not the VaSE algorithm. However, we also propose that the variable width implementation of the algorithm could have caused issues with buckling response. For instance, we observed the beads did not have a stable output, with oscillations in bead width throughout the part instead of uniformity observed in Cura. Such fluctuations could have created additional weakness unaccounted for. The other experiment saw the optimization of a cantilever beam with the goal of maximizing its fundamental natural frequency. The results were post-processed using the VaSE algorithm as well as the geometry extraction method. Measurements showed that VaSE had double the natural frequency of the optimized shape in most cases and at least matched performance in others. Execution of the proposed algorithm is relatively simple, and time required to run it is within a couple of minutes, which is very much comparable with the existing process. In the future, the VaSE infill generation algorithm will be integrated with a commercial slicer for generation of the machine parameters, making it accessible to a wider audience and allowing better functionality.

Author Contributions: Conceptualization, B.K.; methodology, B.K. and P.N.M.; software, P.N.M. and R.A.V.III; validation, B.K., P.N.M. and R.A.V.III; formal analysis, P.N.M. and R.A.V.III; investigation, P.N.M. and R.A.V.III; resources, B.K.; writing—original draft preparation, P.N.M. and R.A.V.III; writing—review and editing, B.K.; funding acquisition, B.K. All authors have read and agreed to the published version of the manuscript.

Funding: This material is based upon work supported by the U.S. Army Combat Capabilities and Development Command–Soldier Center (DEVCOM SC) under Contract Nos. W911QY-20-C-0053 and PR#2025-2110. Any opinions, findings and conclusions or recommendations expressed in this material are those of the author(s) and do not necessarily reflect the views of DEVCOM SC.

Data Availability Statement: Data can be available upon reasonable request to the author.

Conflicts of Interest: The authors declare no conflict of interest.

References

1. Gibson, I.; Rosen, D.; Stucker, B.; Khorasani, M. *Additive Manufacturing Technologies*; Springer International Publishing: Cham, Switzerland, 2021. [CrossRef]

2. Bacciaglia, A.; Ceruti, A.; Liverani, A. Additive Manufacturing Challenges and Future Developments in the Next Ten Years. In *Design Tools and Methods in Industrial Engineering*; Rizzi, C., Andrisano, A.O., Leali, F., Gherardini, F., Pini, F., Vergnano, A., Eds.; Springer International Publishing: Cham, Switzerland, 2020; pp. 891–902. [CrossRef]
3. Dudescu, C.; Racz, L. Effects of Raster Orientation, Infill Rate and Infill Pattern on the Mechanical Properties of 3D Printed Materials. *ACTA Univ. Cibiniensis* **2017**, *69*, 23–30. [CrossRef]
4. Fernandez-Vicente, M.; Calle, W.; Ferrandiz, S.; Conejero, A. Effect of Infill Parameters on Tensile Mechanical Behavior in Desktop 3D Printing. *3D Print. Addit. Manuf.* **2016**, *3*, 183–192. [CrossRef]
5. Cuan-Urquizo, E.; Álvarez-Trejo, A.; Gil, A.R.; Tejada-Ortigoza, V.; Camposeco-Negrete, C.; Uribe-Lam, E.; Treviño-Quintanilla, C.D. Effective Stiffness of Fused Deposition Modeling Infill Lattice Patterns Made of PLA-Wood Material. *Polymers* **2022**, *14*, 337. [CrossRef]
6. Goh, G.D.; Yap, Y.L.; Tan, H.K.J.; Sing, S.L.; Goh, G.L.; Yeong, W.Y. Process–Structure–Properties in Polymer Additive Manufacturing via Material Extrusion: A Review. *Crit. Rev. Solid State Mater. Sci.* **2020**, *45*, 113–133. [CrossRef]
7. Panesar, A.; Abdi, M.; Hickman, D.; Ashcroft, I. Strategies for functionally graded lattice structures derived using topology optimisation for Additive Manufacturing. *Addit. Manuf.* **2018**, *19*, 81–94. [CrossRef]
8. Bendsøe, M.P.; Kikuchi, N. Generating optimal topologies in structural design using a homogenization method. *Comput. Methods Appl. Mech. Eng.* **1988**, *71*, 197–224. [CrossRef]
9. Sigmund, O.; Maute, K. Topology optimization approaches: A comparative review. *Struct. Multidiscip. Optim.* **2013**, *48*, 1031–1055. [CrossRef]
10. Pasko, A.; Fryazinov, O.; Vilbrandt, T.; Fayolle, P.-A.; Adzhiev, V. Procedural function-based modelling of volumetric microstructures. *Graph. Models* **2011**, *73*, 165–181. [CrossRef]
11. Li, D.; Dai, N.; Jiang, X.; Shen, Z.; Chen, X. Density Aware Internal Supporting Structure Modeling of 3D Printed Objects. In Proceedings of the 2015 International Conference on Virtual Reality and Visualization (ICVRV), Xiamen, China, 17–18 October 2015; pp. 209–215. [CrossRef]
12. Fryazinov, O.; Vilbrandt, T.; Pasko, A. Multi-Scale Space-Variant FRep Cellular Structures. *Comput. Aided Des.* **2013**, *45*, 26–34. [CrossRef]
13. Xie, R.; Ulven, C.; Khoda, B. Design and Manufacturing of Variable Stiffness Mattress. *Procedia Manuf.* **2018**, *26*, 132–139. [CrossRef]
14. Karamooz Ravari, M.R.; Kadkhodaei, M.; Badrossamay, M.; Rezaei, R. Numerical Investigation on Mechanical Properties of Cellular Lattice Structures Fabricated by Fused Deposition Modeling. *Int. J. Mech. Sci.* **2014**, *88*, 154–161. [CrossRef]
15. Maskery, I.; Aremu, A.O.; Parry, L.; Wildman, R.D.; Tuck, C.J.; Ashcroft, I.A. Effective design and simulation of surface-based lattice structures featuring volume fraction and cell type grading. *Mater. Des.* **2018**, *155*, 220–232. [CrossRef]
16. Yi, B.; Zhou, Y.; Yoon, G.H.; Saitou, K. Topology optimization of functionally-graded lattice structures with buckling constraints. *Comput. Methods Appl. Mech. Eng.* **2019**, *354*, 593–619. [CrossRef]
17. Yamanaka, D.; Suzuki, H.; Ohtake, Y. Density aware shape modeling to control mass properties of 3D printed objects. In Proceedings of the SIGGRAPH Asia 2014 Technical Briefs, Shenzhen, China, 3–6 December 2014; pp. 1–4. [CrossRef]
18. Aremu, A.O.; Brennan-Craddock, J.; Panesar, A.; Ashcroft, I.; Hague, R.; Wildman, R.; Tuck, C. A voxel-based method of constructing and skinning conformal and functionally graded lattice structures suitable for additive manufacturing. *Addit. Manuf.* **2017**, *13*, 1–13. [CrossRef]
19. Brackett, D.J.; Ashcroft, I.A.; Wildman, R.D.; Hague, R.J.M. An Error Diffusion Based Method to Generate Functionally Graded Cellular Structures. *Comput. Struct.* **2014**, *138*, 102–111. [CrossRef]
20. Cheng, L.; Bai, J.; To, A.C. Functionally Graded Lattice Structure Topology Optimization for the Design of Additive Manufactured Components with Stress Constraints. *Comput. Methods Appl. Mech. Eng.* **2019**, *344*, 334–359. [CrossRef]
21. Yao, Y.; Cheng, L.; Li, Z. A comparative review of multi-axis 3D printing. *J. Manuf. Process.* **2024**, *120*, 1002–1022. [CrossRef]
22. Grigolato, L.; Rosso, S.; Meneghello, R.; Concheri, G.; Savio, G. Design and manufacturing of graded density components by material extrusion technologies. *Addit. Manuf.* **2022**, *57*, 102950. [CrossRef]
23. Murphy, P.N.; Khoda, B. Application of a Continuous Variable Density Infill: Manipulating Center of Gravity. In Proceedings of the ASME 2023 International Design Engineering Technical Conferences and Computers and Information in Engineering Conference, Boston, MA, USA, 20–23 August 2023. [CrossRef]
24. Murphy, P. A Novel Functionally Graded Infill Method for Realizing Topology Optimization for Additive Manufacturing. Master's Thesis, University of Maine, Orono, ME, USA, 2024. Available online: https://digitalcommons.library.umaine.edu/etd/3992 (accessed on 1 January 2025).
25. Ahsan, A.; Xie, R.; Khoda, B. Heterogeneous topology design and voxel-based bio-printing. *RPJ* **2018**, *24*, 1142–1154. [CrossRef]
26. Sigmund, O. A 99 line topology optimization code written in Matlab. *Struct. Multidiscip. Optim.* **2001**, *21*, 120–127. [CrossRef]
27. Özsoy, K.; Erçetin, A.; Çevik, Z.A. Comparison of Mechanical Properties of PLA and ABS Based Structures Produced by Fused Deposition Modelling Additive Manufacturing. *Eur. J. Sci. Technol.* **2021**, 802–809. [CrossRef]

28. Wu, P.; Ramani, K.S.; Okwudire, C.E. Accurate linear and nonlinear model-based feedforward deposition control for material extrusion additive manufacturing. *Addit. Manuf.* **2021**, *48*, 102389. [CrossRef]
29. Chesser, P.; Post, B.; Roschli, A.; Carnal, C.; Lind, R.; Borish, M.; Love, L. Extrusion control for high quality printing on Big Area Additive Manufacturing (BAAM) systems. *Addit. Manuf.* **2019**, *28*, 445–455. [CrossRef]

Disclaimer/Publisher's Note: The statements, opinions and data contained in all publications are solely those of the individual author(s) and contributor(s) and not of MDPI and/or the editor(s). MDPI and/or the editor(s) disclaim responsibility for any injury to people or property resulting from any ideas, methods, instructions or products referred to in the content.